AFRL-RX-WP-JA-2016-0198

HYBRID CO-DEPOSITION OF MIXED-VALENT MOLYBDENUM-GERMANIUAM OXIDES (MoxgEYoZ): A ROUTE TO TUNABLE OPTICAL TRANSMISSION (POSTPRINT)

Neil R. Murphy and John G. Jones
AFRL/RX

Lirong Sun and John T. Grant
General Dynamics Information Technology

3 MARCH 2015
Interim Report

(STINFO COPY)

AIR FORCE RESEARCH LABORATORY
MATERIALS AND MANUFACTURING DIRECTORATE
WRIGHT-PATTERSON AIR FORCE BASE, OH 45433-7750
AIR FORCE MATERIEL COMMAND
UNITED STATES AIR

REPORT DOCUMENTATION PAGE

Form Approved
OMB No. 0704-0188

1. REPORT DATE *(DD-MM-YY)*	2. REPORT TYPE	3. DATES COVERED *(From - To)*
3 February 2015	Interim	16 November 2012 – 3 February 2015

4. TITLE AND SUBTITLE

HYBRID CO-DEPOSITION OF MIXED-VALENT MOLYBDENUM-GERMANIUAM OXIDES ($Mo_xGe_yO_z$): A ROUTE TO TUNABLE OPTICAL TRANSMISSION (POSTPRINT)

5a. CONTRACT NUMBER
FA8650-09-D-5430-0024

5b. GRANT NUMBER

5c. PROGRAM ELEMENT NUMBER
63112F

6. AUTHOR(S)

1) Neil R. Murphy and John G. Jones – AFRL/RX

2) Lirong Sun and John T. Grant - General Dynamics Information Technology

5d. PROJECT NUMBER
2100

5e. TASK NUMBER 0024

5f. WORK UNIT NUMBER
X0LX

7. PERFORMING ORGANIZATION NAME(S) AND ADDRESS(ES)

1) AFRL/RX, 3500 Hobson Way, Wright Patterson AFB, Dayton, OH 45433

2) GDIT 3211 Jermantown Road, Fairfax, VA 22030

8. PERFORMING ORGANIZATION REPORT NUMBER

9. SPONSORING/MONITORING AGENCY NAME(S) AND ADDRESS(ES)

Air Force Research Laboratory
Materials and Manufacturing Directorate
Wright-Patterson Air Force Base, OH 45433-7750
Air Force Materiel Command
United States Air Force

10. SPONSORING/MONITORING AGENCY ACRONYM(S)
AFRL/RXAP

11. SPONSORING/MONITORING AGENCY REPORT NUMBER(S)
AFRL-RX-WP-JA-2016-0198

12. DISTRIBUTION/AVAILABILITY STATEMENT
Distribution Statement A. Approved for public release: distribution unlimited.

13. SUPPLEMENTARY NOTES
PA Case Number: 88ABW-2015-00396; Clearance Date: 3 Feb 2015. This document contains color. Journal article published in Journal of Applied Crystallography, Vol. 590, 1 September 2015. © 2015 Elsevier B.V. The U.S. Government is joint author of the work and has the right to use, modify, reproduce, release, perform, display, or disclose the work.
The final publication is available at http://dx.doi.org/10.1016/j.tsf.2015.08.005

14. ABSTRACT ***(Maximum 200 words)***

Mixed-valent oxides of molybdenum and germanium were deposited simultaneously using reactive magnetron co-deposition within an oxygen–argon environment. The films' stoichiometry, optical, and physical properties were varie through changes in oxygen partial pressure induced by systematic variation of the potential applied to themolybdenumcathode. The oxygen partial pressurewas determined fromthe drop in pressure asmeasured by a capacitance manometer, assuming constant argon partial pressure. To facilitate deposition, a constant power of 100WDCwas applied to the germaniumcathode,while powerwas applied to the molybdenumtarget using a modulated pulse power supply. Modulated pulse power magnetron sputtering was used due to its ability to generate high target power densities, allowing for rapid reduction of oxygen on the surface of the "oxygen poisoned molybdenum cathode, as well as for its highly metallic plasma resulting in increased oxygengettering capability. Changes in the modulated pulse power supply's capacitor bank voltage load, stepped from settings of 300 to 380 V, resulted in films ranging from mixtures of transparent GeO2 (Ge4+) and MoO3 (Mo6+) to the introduction of various absorptive ionic species includingMo5+,Mo4+, Ge2+ and Ge0, as determined from X-ray photoelectron spectroscopy.

15. SUBJECT TERMS
Magnetron sputtering, Ellipsometry, X-ray photoelectron spectroscopy, Mixed oxides, Germanium oxide, Molybdenum oxide

16. SECURITY CLASSIFICATION OF:			17. LIMITATION OF ABSTRACT:	18. NUMBER OF PAGES	19a. NAME OF RESPONSIBLE PERSON (Monitor)
a. REPORT	b. ABSTRACT	c. THIS PAGE			Byron Edmonds
Unclassified	Unclassified	Unclassified	SAR	14	19b. TELEPHONE NUMBER *(Include Area Code)* (937) 255-9638

Thin Solid Films 590 (2015) 248–259

Contents lists available at ScienceDirect

Thin Solid Films

journal homepage: www.elsevier.com/locate/tsf

Hybrid co-deposition of mixed-valent molybdenum–germanium oxides ($Mo_xGe_yO_z$): A route to tunable optical transmission

Neil R. Murphy [a,*], Lirong Sun [b], John G. Jones [a], John T. Grant [b]

[a] Air Force Research Laboratory, Materials and Manufacturing Directorate, Wright-Patterson Air Force Base (WPAFB), Dayton, OH 45433, USA
[b] General Dynamics Information Technology, 5100 Springfield Street, Dayton, OH 45431, USA

ARTICLE INFO

Article history:
Received 13 February 2015
Received in revised form 6 August 2015
Accepted 6 August 2015
Available online 8 August 2015

Keywords:
Magnetron sputtering
Ellipsometry
X-ray photoelectron spectroscopy
Mixed oxides
Germanium oxide
Molybdenum oxide
Thin film
Optical characterization

ABSTRACT

Mixed-valent oxides of molybdenum and germanium were deposited simultaneously using reactive magnetron co-deposition within an oxygen–argon environment. The films' stoichiometry, optical, and physical properties were varied through changes in oxygen partial pressure induced by systematic variation of the potential applied to the molybdenum cathode. The oxygen partial pressure was determined from the drop in pressure as measured by a capacitance manometer, assuming constant argon partial pressure. To facilitate deposition, a constant power of 100 W DC was applied to the germanium cathode, while power was applied to the molybdenum target using a modulated pulse power supply. Modulated pulse power magnetron sputtering was used due to its ability to generate high target power densities, allowing for rapid reduction of oxygen on the surface of the "oxygen poisoned" molybdenum cathode, as well as for its highly metallic plasma resulting in increased oxygen-gettering capability. Changes in the modulated pulse power supply's capacitor bank voltage load, stepped from settings of 300 to 380 V, resulted in films ranging from mixtures of transparent GeO_2 (Ge^{4+}) and MoO_3 (Mo^{6+}) to the introduction of various absorptive ionic species including Mo^{5+}, Mo^{4+}, Ge^{2+} and Ge^0, as determined from X-ray photoelectron spectroscopy. The presence of each of the aforementioned ions results in characteristic changes in the films' band energies and optical absorption. As deposited $Mo_xGe_yO_z$ thin films grown using this method have been shown to have optical gap energies that are able to be tailored between 3.57 eV and 0.18 eV, spanning useful ranges for devices operating in the visible and near-infrared.

Published by Elsevier B.V.

1. Introduction

Multi-component oxide thin films have found uses in several applications spanning the fields of optics and electronics. Some examples of the multitude of uses for these materials include transparent conductive oxides, such as aluminum zinc oxide [1–3] and indium tin oxide [3–5], switchable electrochromic smart windows [6–8], flat panel displays [9–12], and optical coating designs requiring mixtures of high and low refractive index materials, such as rugate filters [13,14] and infrared reflectors [1]. While most of these applications require fully stoichiometric, transparent oxide mixtures, recent works exploring substoichiometric oxide systems have generated interest due to their unique absorptive properties [15–17]. Specifically, studies by Gil-Rostra et al. [15,17–19] have utilized reactive magnetron sputtering to tailor the visible absorption of substoichiometric transition metal oxides, including Ni [15], Co [15,19], Fe [15], Cu [15,18], W [15,17], and Mo [15], within a dielectric silicon dioxide matrix. Gil-Rostra et al. were able to deposit a variety of colorful "ionic glass" thin films by varying the fraction, and chemistry, of transition metal cations within the SiO_2 matrix [15,20–22]. Specifically, the visible absorption characteristics associated with transition metal coordination complexes, perceived as color by the human eye, are attributed to the splitting of d-electron energy levels as a result of metal–ligand bonding [23,24]. The ability to systematically leverage the visible absorption of thin film coatings has several advantages for the development of coatings for ophthalmic usage [17,19,25], photovoltaics [4,26–29], light emitting diode components [30–32], and plasmonics, providing a potential alternative to lossy metal-based configurations [33–35].

To properly facilitate sputter deposition of mixed-valent ionic glasses, two distinct materials must be selected. Materials required include a stable, dielectric matrix, as well as an easily reducible transition metal oxide. Typically, the selection of the metallic species is limited to those transition metals and lanthanides that have unfilled d and f electron shells, respectively, which give rise to visible absorption as a result of excitation energies ranging from ~1 to 3 eV ($\lambda \approx 400$–1240 nm) [23,24,36]. Given that these materials will be deposited simultaneously, it is also necessary that the intended matrix phase is able to form a fully stoichiometric oxide, without also leading to full oxidation of the absorbing constituents, potentially rendering them transparent to visible

* Corresponding author at: Air Force Research Laboratory, Materials & Manufacturing Directorate, 3500 Hobson Way, Wright-Patterson AFB, OH 45433, USA.
E-mail addresses: neil.murphy.1@us.af.mil (N.R. Murphy), lirong.sun.2.ctr@us.af.mil (L. Sun), John.jones.66@us.af.mil (J.G. Jones), john.grant.5.ctr@us.af.mil (J.T. Grant).

http://dx.doi.org/10.1016/j.tsf.2015.08.005
0040-6090/Published by Elsevier B.V.

wavelengths. The likelihood of disparate materials bonding to form coordination compounds, transparent or otherwise, is governed by the enthalpy of formation, which represents the thermodynamic driving force for reactivity. The Ge–O and Mo–O systems are of interest due to the fact that the enthalpies of formation of substoichiometric MoO_2 (relative to MoO_3) and stoichiometric GeO_2 are very similar at room temperature, $\Delta_f H^o_{(MoO2)} = -588$ kJ/mol and $\Delta_f H^o_{(GeO2)} = -580$ kJ/mol [37], a potential indicator that these two compounds can be deposited concurrently. In addition to MoO_2 (Mo^{4+}), the facile reduction of MoO_3 can lead to the formation of Mo_2O_5, and the corresponding ionic species, Mo^{5+} [38–40]. Therefore, it should be possible to control the relative amounts of absorptive, substoichiometric MoO_x ($0 < x < 3$) coordination compounds within a transparent GeO_2 matrix.

Several methods employing reactive magnetron sputtering have been studied for depositing both stoichiometric and substoichiometric mixed oxide thin films. Methods used for depositing mixed oxides include the use of alloyed targets [41–45], affixing strips of various materials to the target surface [15,17–19], and co-deposition using multiple sources [46–49]. While each of these methods is capable of depositing uniform, high quality thin films, co-deposition was selected for use within this study. Justification for the use of co-deposition is due to the dynamic experimental environment associated with the use of two separate magnetron sources, which allows for independent variation of power application, magnet configuration, working distance, and target diameter. Unlike previous studies of co-deposited mixed oxide systems, this study utilizes an ionized physical vapor deposition technique known as modulated pulse power magnetron sputtering (MPPMS). MPPMS was used due to its ability to generate high target power densities, allowing for rapid reduction of oxygen on the surface of the "oxygen poisoned" molybdenum cathode, as well as for its highly metallic plasma resulting in increased oxygen-gettering capability [50–53]. Therefore, fine adjustments in the applied MPPMS power should be able to accurately control the oxygen partial pressure within the deposition chamber via chemisorption [50,54–57].

This work uses a scalable co-deposition method that allows for the precise control of oxygen partial pressure in order to achieve controlled variation in both the composition and chemical state of mixed $Mo_xGe_yO_z$ thin films. This work also explores the reduction pathway of the oxide compounds present within the deposited films, and provides a detailed correlation between processing parameters, chemical properties and optical behavior. Finally, the methods outlined within this study are intended to serve as a template for the deposition and exploration of other substoichiometric mixed-oxide systems.

2. Experimental

2.1. Fabrication

$Mo_xGe_yO_z$ films were deposited within a stainless steel high-vacuum chamber equipped with two diametrically opposed magnetron sources aligned in a confocal arrangement. Two unbalanced, 50 mm diameter magnetron sources with equivalent magnetic field strengths were used in this work. The first magnetron (K.J. Lesker Torus®) was equipped with a 50 mm germanium (Plasmaterials, 99.999% purity) sputter target. The second magnetron (Meivac MAK®) was equipped with a 50 mm molybdenum target (Plasmaterials, 99.95%). Both magnetrons were positioned at a 20° angle with respect to the substrate normal. Substrates, both prime grade (001) p-type silicon (University Wafer LLC) and 1.65 mm thick fused quartz (Machine Glass Specialists Inc.) were loaded into the chamber through a load-lock system. Substrates were placed upon an unheated holder set to rotate at 12 rpm to reduce anisotropy imparted by the sputtering process. The position of the magnetrons was set to ensure a target-to-substrate distance of 13 cm. Substrates were covered with a shutter to shield against spurious droplets at the onset of sputtering.

Prior to plasma ignition, the chamber was evacuated to a pressure of 6.6×10^{-5} Pa, or better, using a turbomolecular pump in conjunction with a mechanical roughing pump. Upon achieving the required base pressure, argon (99.999%) was introduced into the vacuum chamber at a flow rate (Q_{Ar}) of 25 sccm using a mass flow controller. The pressure of the argon gas (P_{Ar}), measured using a capacitance manometer, was set at 1.33 Pa and maintained constant by locking the gate valve position. The static gate valve resulted in a constant pumping speed of approximately 32 L/s. P_{Ar} was expected to be constant throughout all depositions, assuming a negligible amount of argon loss through ion implantation at the target surfaces. Once P_{Ar} was stabilized at 1.33 Pa, oxygen (99.999%) was introduced through a separate mass flow controller. The oxygen partial pressure, P_{O2}, was determined by subtracting P_{Ar} from the total chamber working pressure P_{TOT}. The oxygen flow rate (Q_{O2}) was first stepped from 0 to 10 sccm, in 1 sccm increments. Adjustment of Q_{O2} took place in order to determine the onset of the "poisoned" regime, ensuring sufficient oxygen levels to correspond to fully oxidized films. The value of Q_{O2} was set to 6 sccm resulting in a total flow rate (Q_{TOT}) of 31 sccm. Justification for the selection of Q_{O2} can be found in Section 3 below. Note that the gases were not mixed prior to entering the chamber. Oxygen was introduced through a port near the substrate holder, while argon was introduced near the top of the chamber, in the vicinity of the magnetron sources.

The plasma was generated using two separate power supplies; an Advanced Energy MDX 500 power supply was used for the germanium source, while a ZPulser Axia 180 MPPMS power supply was used for the molybdenum source. Germanium sputtering took place at a constant power of 100 W, and molybdenum deposition via MPPMS was carried out with specific capacitor bank voltage loads (U_L) that were systematically varied from 0 to 380 V. MPPMS discharge events, lasting 1 ms at a frequency of 100 Hz, resulted in a duty cycle of 10%. The 1 ms pulse was separated into two different regimes, similar to the pulse profiles used by Hála et al. [50]. The first stage of the pulse generated a low energy plasma discharge with a duration of 400 μs derived from a 20% micropulse duty cycle, and the second stage consisted of a higher energy plasma lasting 600 μs controlled by micropulses applied at a 54.5% duty cycle with an on time of 12 μs and an off time of 10 μs. Temporal cathode voltage and current output were monitored using a Tektronix DPO 5204 multi-channel oscilloscope. Films were deposited on 50 mm diameter silicon substrates and 25 mm diameter quartz witness samples for a total of 3 min, resulting in thicknesses ranging from 220 to 300 nm. In the case of samples prepared for X-ray reflectivity, the deposition time was held for 1 min to ensure an appropriate thickness (≤100 nm).

2.2. Characterization

The composition, chemistry, optical properties, and structure of as deposited $Mo_xGe_yO_z$ thin films were studied using a combination of grazing incidence X-ray diffraction (GIXRD), X-ray reflectivity (XRR), X-ray photoelectron spectroscopy (XPS), spectroscopic ellipsometry (SE), and ultraviolet–visible-near-infrared optical spectrophotometry (UV–Vis–NIR).

Structural properties of the as-deposited $Mo_xGe_yO_z$ films, including roughness, thickness, crystallinity, and density, were measured using GIXRD and XRR. Both GIXRD and XRR measurements were performed with a Rigaku SmartLab X-ray diffractometer using a Cu-Kα (1.5418 Å) source. GIXRD measurements of films deposited on Si(100) wafers were taken within a 2θ range of 15–80° at a rate of 0.1°/s. XRR scans were obtained for 2θ values between 0.0° and 6.0° with a step size of 0.005°. Raw XRR data were fit within the Rigaku Globalfit software package.

XPS analysis was used to measure both the composition and chemical valence states of the compounds present in the films. XPS measurements were performed using a Physical Electronics 5700 equipped with a monochromatic Al Kα (1486.6 eV) X-ray source. Compositional

analysis took place using survey scans at an analyzer pass energy of 187.85 eV from 0 to 1400 eV binding energy, while an analyzer pass energy of 29.35 eV was used for high energy resolution measurements to determine the chemical valence states of the deposited species. For convenience, all spectra were calibrated with respect to the adventitious carbon 1 s transition at a binding energy (BE) of 284.6 eV. The presence of adventitious carbon is the result of atmospheric exposure during transportation from the deposition system to the analysis chamber. High energy resolution scans were fit with Gaussian–Lorentzian line shapes after Shirley background subtraction. Processing of XPS spectra was performed using the CasaXPS 2.3.16 software package [58].

The optical properties of the $Mo_xGe_yO_z$ films were evaluated using a J.A. Woollam VASE spectroscopic ellipsometer in both transmission (T) and SE modes over a wavelength range of 255–1700 nm (4.86–0.72 eV). A single model was used to simultaneously fit both transmitted intensity and variable angle SE data in order to ensure precise, unique solutions for the refractive index, extinction coefficient, and thickness of the absorbing thin films [59]. Most importantly, the use of the VASE instrument's transmission mode, measuring transmitted intensity at normal incidence through the film and substrate, allows for increased precision in determining the onset of absorption attributed to the optical band gap. Raw ellipsometry data is gathered by monitoring the changes in both the magnitude (Ψ) and phase difference (Δ) of polarized light after interaction with the sample surface at angles of incidence of 50°, 55°, and 60°. The spectral refractive index ($n(\lambda)$), the extinction coefficient ($k(\lambda)$), and the thickness of the films were calculated by simultaneously fitting raw T and SE data with a Kramers–Kronig consistent optical model, described in detail in Section 3.4. T data was weighted 2:1 versus SE data and the optical model was optimized in order to minimize the resulting mean squared error (MSE) through iterative adjustment of the fitting parameters using the Levenberg–Marquardt method, improving the fit quality [59]. Fits with an MSE greater than 25 were rejected.

3. Results and discussion

3.1. Establishment of conditions

The oxygen partial pressure (P_{O2}), as a function of flow rate (Q_{O2}), was carefully monitored prior to deposition with both magnetron sources. As mentioned previously, the partial pressure of argon (P_{Ar}) was set to 1.33 Pa and then oxygen was introduced into the deposition chamber. Pumping speeds were calculated by analyzing the working pressure as a function of Q_{O2} prior to plasma ignition in order to ensure no reduction in P_{O2} through oxide formation due to chemisorption.

Using only the Ge source, a plot of (P_{O2}) versus Q_{O2} is shown in Fig. 1. The pumping speed ($S = Q_{TOT}/P_{TOT}$) attributed to each set of P_{TOT} vs. Q_{TOT} was calculated, resulting in an average rate of 32 L/s. P_{TOT} was then evaluated as a function of Q_{O2} with the germanium source operating at 100 W DC, in order to establish the locations of the gettering, transition, and poisoned regimes associated with the reactive sputtering process for Ge [51,55,60,61]. As demonstrated in Fig. 1, the value of P_{O2} at $Q_{O2} = 0.0$ is 0 Pa, validating the assumption of constant argon pressure during sputtering. As Q_{O2} increases to 1 sccm, there is no change in P_{O2}, indicating that all available oxygen is effectively chemisorbed. Changes in P_{O2}, associated with the presence of gaseous oxygen, begin to arise at $Q_{O2} \geq 2$ sccm. Increases in P_{O2} for $1 < Q_{O2} \leq 5$ sccm signify the onset of the transition regime, wherein the germanium deposition flux is unable to fully react with the available oxygen, leading to the gradual oxidation of the target, substrate, and adjacent surfaces. Note the mild hysteresis occurring within the transition region in Fig. 1; this commonly reported behavior is associated with the oxidation and reduction of the sputter target surface as reactive gas content is varied [55–57,60–62]. At Q_{O2} values near 5 sccm and above, P_{O2} increases linearly at a rate proportional to the pumping speed of the system. The linear behavior of P_{O2} above 5 sccm can be attributed to the saturation of both the

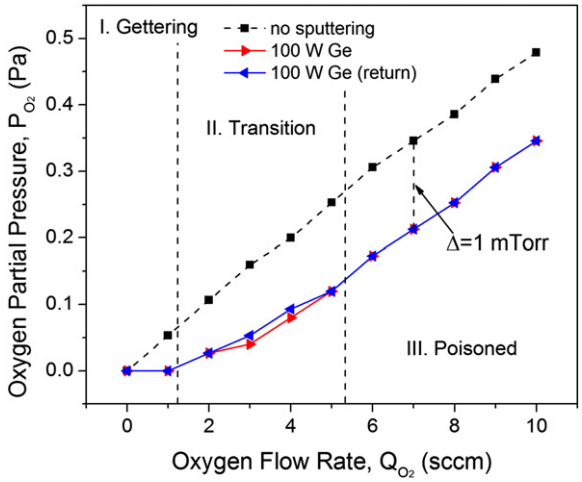

Fig. 1. Total working pressure as a function of oxygen flow rate (P_{O2}) for increasing (red triangles) and decreasing (blue triangles) oxygen flow rates for sputtering from a Ge target. Note that the pressure was also measured as a function of flow rate under ambient conditions (black squares).

Ge target and collecting surfaces with chemisorbed oxygen; therefore, excess oxygen can only be removed through the pumping system. The identification of the onset of the poisoned regime for Ge is associated with the formation of fully stoichiometric GeO_2.

The goal of this work requires the initial deposition of transparent, dielectric GeO_2 and MoO_3, followed by the incorporation of optically absorbing metal-oxide coordination complexes associated with sub-stoichiometric oxide formation characteristic of transition mode sputtering [55–57,60–62]. Therefore, deposition of mixed-valent molybdenum and germanium oxides must take place within the transition regime, leveraging the high metallic target flux associated with the MPP process to control the oxygen partial pressure, and subsequently, the composition and chemistry of the deposited films [50,54,63].

Having identified the onset of target poisoning for germanium deposition, characterization of the P_{O2} vs. Q_{O2} behavior for the co-deposition from Ge and Mo targets was performed using Q_{O2} values of 4, 6, and 8 sccm. P_{TOT} values corresponding to $Q_{O2} = 4$, 6, and 8 sccm were recorded as a function of U_L applied to the molybdenum sputter source; note that the germanium source was operated concurrently at 100 W DC. A plot of P_{O2} vs. U_L, shown in Fig. 2, demonstrates significant differences in behavior for Q_{O2} values of 4, 6, and 8 sccm. As expected, P_{O2} values shown in Fig. 2 decrease as a function of increasing U_L due to

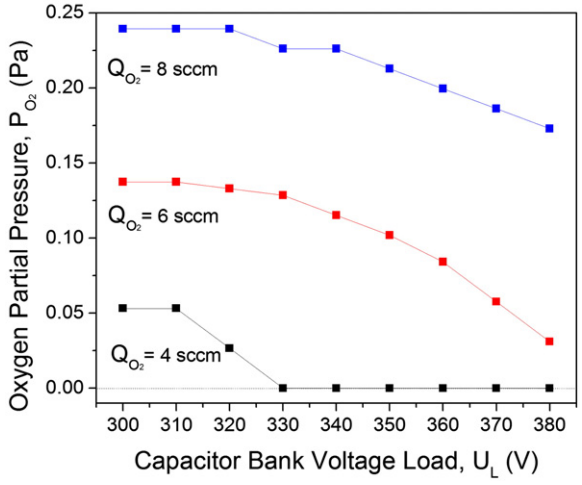

Fig. 2. Plot of oxygen partial pressure (P_{O2}) as a function of MPP capacitor bank voltage load (U_L).

oxygen uptake associated with the additional molybdenum deposition flux. Based on the data in Fig. 2, the onset of the transition regime is demonstrated by the characteristic decrease in P_{O2} as a function of increasing U_L.

The relatively flat behavior of P_{O2} at lower U_L values is attributed to the inability to fully react with the excess oxygen present within the chamber, consistent with the poisoned regime. As U_L increases, the pressure begins to decrease due to the higher levels of molybdenum deposition flux brought on by the augmentation of U_L. Since U_L is directly related to the magnitude of the discharge voltage, depicted in Fig. 3a, increases in U_L are responsible for augmenting the kinetic energy of incident Ar^+ ions responsible for sputtering. Therefore, further increases in U_L lead the reduction of oxides formed on the target surfaces, giving way to the onset of transition mode sputtering, as demonstrated by the decrease in P_{O2} and P_{TOT}. As shown in Fig. 3a, the slope of the voltage discharge at $t > 1$ ms begins to increase as the target surface becomes more metallic. The gettering regime is easily identified due to the fact that all oxygen present within the chamber is chemisorbed by the adatoms from the deposition flux, therefore there will be a net P_{O2} of 0.00 Pa, corresponding to $P_{Ar} = 1.33$ Pa. The onset of gettering is clear for $Q_{O2} = 4$ sccm, at 330 V (Fig. 2), while Q_{O2} values of 6 and 8 sccm correspond to P_{O2} levels that are unable to be fully chemisorbed by the deposition flux even at $U_L = 380$ V. The resulting augmentation of the molybdenum deposition flux is associated with both an increase in both discharge current (Fig. 3b) and photoemission attributed to excited molybdenum species (Mo I) (Fig. 3c). Current and voltage values for the Ge and Mo sputter sources can be found in Tables 1 and 2, respectively. Note, the U_L value of 380 V corresponds to an average current of approximately 0.7 A; higher U_L settings could not be used due to the thermal constraints of the magnetrons. The levels of P_{O2}, for $Q_{O2} = 6$ sccm, are shown to have sufficient sensitivity to U_L to allow for reduction of the oxygen content in the chamber, while still retaining stability over a wide range of partial pressures (Fig. 2). As a result of this analysis, $Q_{O2} = 6$ sccm was selected for the deposition of $Mo_xGe_yO_z$ films.

Table 1
DC cathode voltage, current, and power output of germanium sputter source in response to changes in U_L applied to the molybdenum cathode during co-deposition.

U_L (V)	DCMS germanium		
	Voltage (V)	Current (I)	Power (W)
300	520	0.190	98.8
310	523	0.190	99.4
320	522	0.190	99.2
330	522	0.190	99.2
340	519	0.190	98.6
350	516	0.190	98.0
360	513	0.192	98.5
370	513	0.193	99.0
375	511	0.194	99.1
380	506	0.196	99.2

3.2. Structure and morphology

Measurement of the crystallinity of $Mo_xGe_yO_z$ thin films indicated that all films deposited were XRD amorphous, as evidenced by the presence of the lack of diffraction peaks as well as the broad amorphous humps shown in Fig. 4. Similar amorphous character has been reported by Mohamed et al. for sputter deposited MoO_3, demonstrating broad amorphous humps with centroids moving from $2\theta = 27°$ to $2\theta = 38°$ as the oxygen partial pressure is decreased from 0.16 to 0.022 Pa [64]. The lack of long-range structural order within these films can be attributed to low adatom mobility related to the low deposition temperature ($T \leq 100$ °C), interruption of film nucleation via the formation of a surface coating layer [65–67], and incompatibility of mixing between the germanium and molybdenum oxide compounds [68,69]. The amorphous structure of multi-component oxide coatings deposited at room temperature has also been reported by Gil-Rostra et al. for a variety of mixed-valent films [15,17–19].

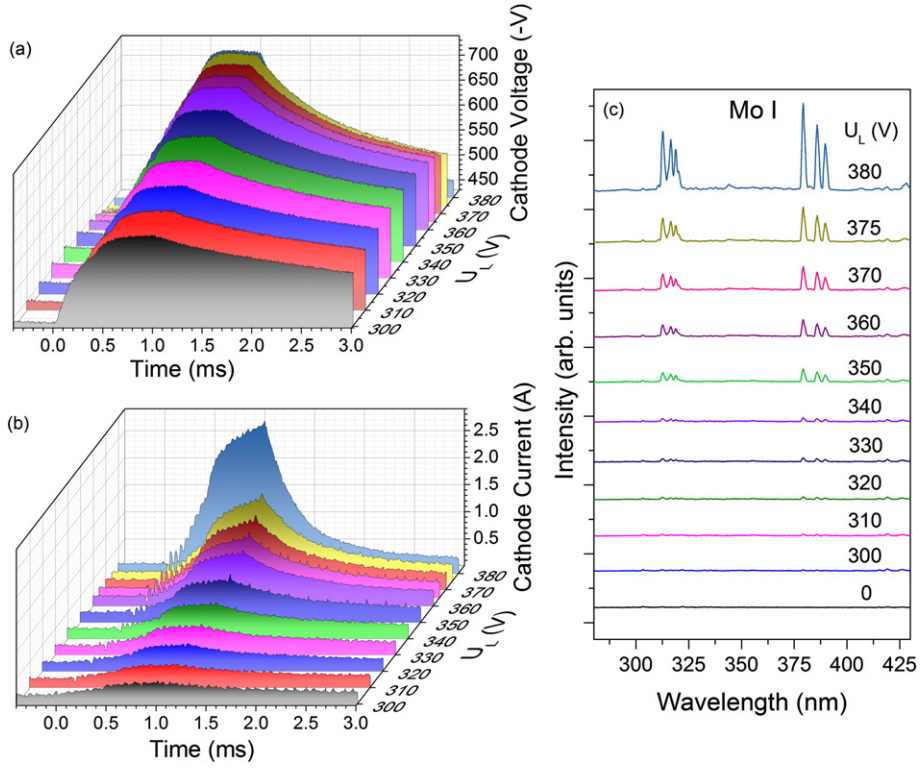

Fig. 3. Temporal evolution of (a) voltage and (b) current associated with the molybdenum cathode during the MPPMS pulse. Photoemission events attributed to the excited molybdenum (Mo I) are shown in (c). Spectra are offset for clarity.

Table 2
DC cathode voltage, current, and power output of molybdenum sputter source as a function of U_L.

U_L (V)	MPPMS molybdenum					
	Peak voltage (V)	Peak current (I)	Peak power (W)	Average voltage (V)	Average current (I)	Average power (W)
300	−614	0.441	270.5	−524	0.261	136.9
310	−632	0.446	282.1	−536	0.265	142.1
320	−649	0.522	338.6	−546	0.283	154.4
330	−669	0.581	388.9	−555	0.298	165.6
340	−685	0.683	468.3	−562	0.333	186.7
350	−705	0.903	636.9	−566	0.374	211.4
360	−718	1.039	746.4	−563	0.406	228.4
370	−732	1.384	1013.8	−556	0.471	261.8
375	−739	1.642	1213.4	−546	0.518	283.3
380	−728	2.825	2055.5	−494	0.712	351.4

XRR measurements were performed to probe the density, thickness, and roughness of the $Mo_xGe_yO_z$ films deposited at U_L values of 300 to 380 V. XRR is able to provide in estimation of the density based on the location of the critical angle (θ_c), below which, the total reflection of incident X-rays occurs [70]. In addition to density, film thickness can be calculated based on the period of oscillations known as Kiessig fringes [70]. Finally, surface and interface roughness values can be determined as a function of the decay in X-ray signal, attributed to scattering losses at increasing values of 2θ [70]. The model used for XRR fitting and calculation consisted of a silicon substrate with a 2 nm native SiO_2 layer, an interfacial roughness layer, and finally a homogeneous layer of unconstrained density, thickness and surface roughness. The assumption of a homogeneous film microstructure, comprised of a random solid solution of metallic cations within a germanium oxide matrix, is based upon reports by Gil-Rostra et al. for similar mixed oxide systems [15,17–19]. Based on the data shown in Fig. 5, the behavior of the reflected X-ray intensity shows an increase in θ_c with increasing capacitor bank voltage, indicating densification as a function of increasing voltage. Simulated XRR spectra indicate good agreement between experimentally obtained values and model assumptions, as shown in Fig. 5. Roughness values remained relatively stable as a function of U_L, varying between 0.5 and 2.0 nm, while calculated densities (Fig. 6) demonstrate a non-linear increase as a function of U_L. Note that the calculated density rises from 3.2 to 6.4 g/cm^3 as U_L is increased from 300 to 380 V. The initial low density values, at $300 \le U_L \le 350$ can be attributed to the relatively high amount of residual oxygen present within the chamber (Fig. 2), resulting in the growth of fully oxidized

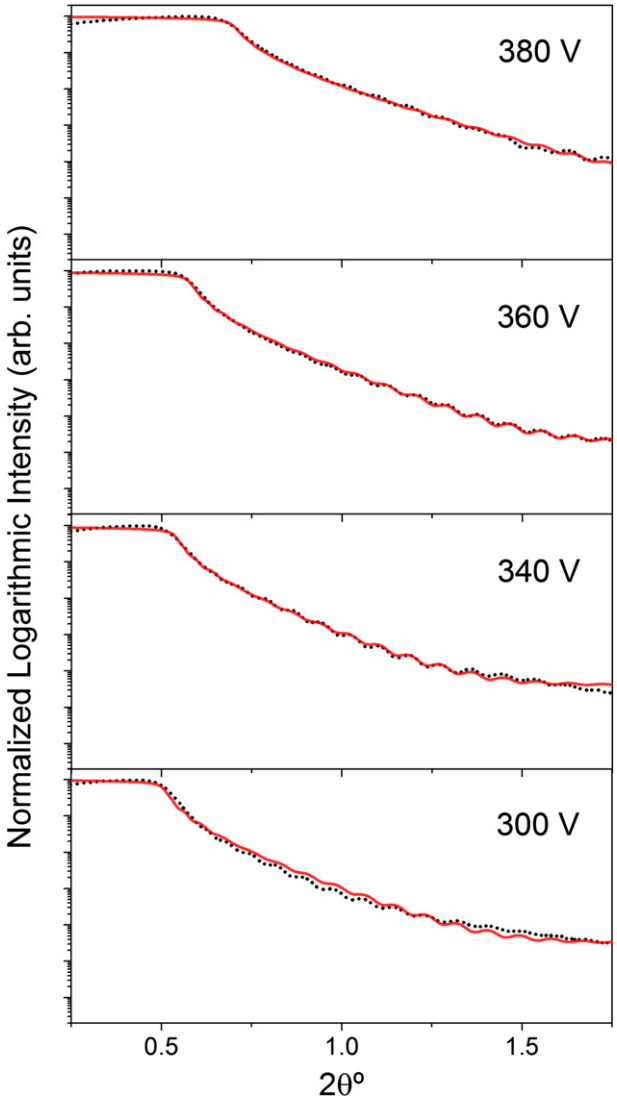

Fig. 5. Selected XRR measurements (black dotted line) and model calculations (semi-transparent red line) for determination of thickness, roughness, and density.

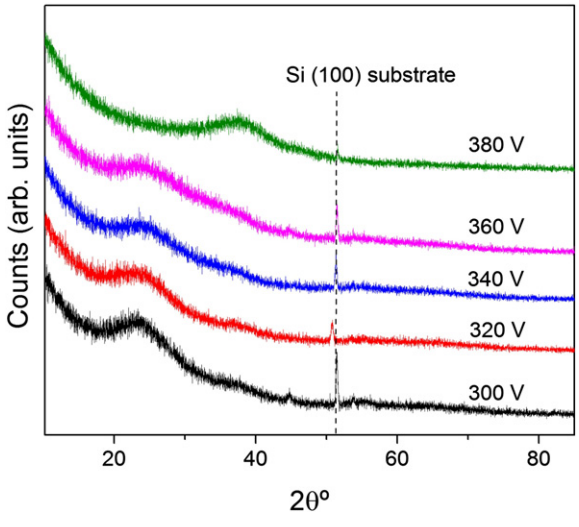

Fig. 4. Raw grazing incidence X-ray diffraction patterns from $Mo_xGe_yO_z$ thin films for selected values of U_L. Diffraction patterns are offset for clarity.

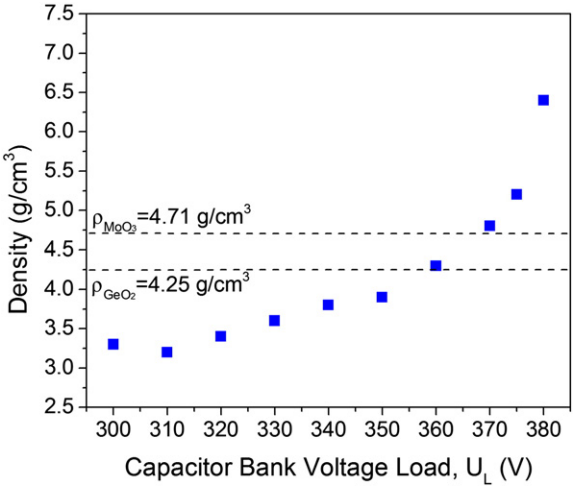

Fig. 6. Density measurements as a function of MPP capacitor bank voltage load (U_L).

films. However, the densities of the oxygen-rich films within the $300 \le U_L \le 350$ region are significantly lower than that of their bulk constituents [37,64,71–73]. The discrepancy between bulk densities for GeO_2 and MoO_3 and those of the as-deposited films can be attributed to no heating being applied to the substrate during deposition as well as the tendency of oxygen to act as a grain refining agent, interrupting nucleation and leading to high defect and interface volumes [65–67]. The low densities calculated through XRR measurement and modeling are consistent with the amorphous structure of the films, as evinced by the lack of crystalline character shown by the GIXRD measurements in Fig. 4. The increases in density obtained for higher values of U_L resulted from the growth of higher density, sub-stoichiometric compounds associated with the drop in P_{O2} at $350 \le U_L$.

3.3. Measurement of $Mo_xGe_yO_z$ composition and valence state

XPS survey scans, shown in Fig. 7 for U_L values of 300 and 380 V, were performed in order to determine the atomic concentrations of the constituents. The core level transitions used were O 1s, Mo 3d, Ge $2p_{3/2}$ and C 1s. Compositions from, and binding energies of, these transitions are included in Table 3. As demonstrated in Fig. 7, the concentrations of the constituent elements vary significantly for U_L values of 300 and 380 V. Films deposited at $U_L = 300$ V were found to contain approximately 3% C, 68% O, 4% Mo and 25% Ge, while films deposited at $U_L = 380$ V had 22% C, 48% O, 15% Mo and 15% Ge. The decreased oxygen content, and the increased ratio of molybdenum to germanium, are representative of the augmentation of the molybdenum flux attributed to higher U_L values.

High energy resolution XPS measurements of the Ge 3d (Fig. 8) and Mo 3d (Fig. 9) spectra were acquired for U_L values from 300 to 580 V in addition to survey spectra. Measurement and analysis of high energy resolution XPS spectra were conducted in order to gain understanding of the oxidation states present within the deposited films. XPS data for the Ge 3d (Fig. 8) and Mo 3d transitions (Fig. 9) indicate changes in oxidation states in response to the decreased levels of P_{O2} brought on by increases in U_L. Beginning with the Ge 3d transition, incremental changes in U_L from 300 to 370 V are associated with spectra centered at BE = 32.8 eV, consistent with published values for the Ge^{4+} cation associated with tetrahedral GeO_2 [72,74]. As U_L is increased further, to 375 V, the evolution of the Ge^{2+} cation, attributed to the presence of trigonal planar GeO can be observed at BE = 31.0 eV in addition to the GeO_2 [72,74,75]. Note, the trigonal planar arrangement of GeO is the result of sp^2 hybridization between Ge and O energy levels [75,76]. Finally, conditions correlated to $U_L = 380$ V led to the deposition of GeO_2, GeO, and elemental Ge^0 (BE = 29.0 eV). Thus, chemical shifts associated with the formation of GeO_2, GeO, and Ge were shown to occur only at values of U_L corresponding to $P_{O2} \le 0.05$ Pa.

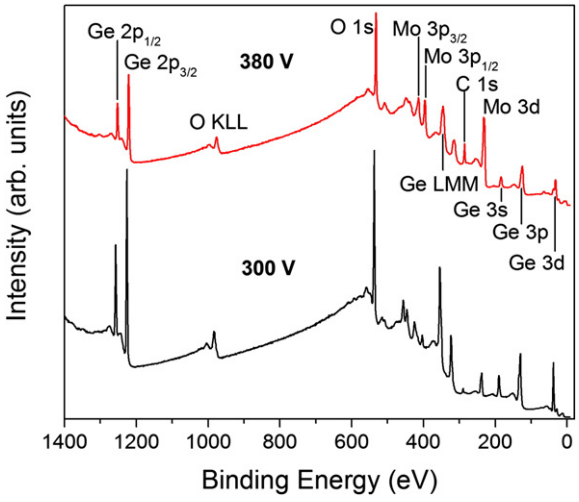

Fig. 7. XPS survey scans for $Mo_xGe_yO_z$ films deposited for U_L values of 380 V (top) and 300 V (bottom) spectra are offset for clarity. $U_L = 380$ V is associated with enhanced ratios of Mo:O.

Table 3
Composition and raw binding energies of core level transitions obtained from XPS survey scans. Concentrations are not accurate to three significant figures, but they are shown to allow easier comparisons of data.

U_L (V)	C 1s		O 1s		Mo 3d		Ge $2p_{3/2}$	
	Binding energy (eV)	at.%	Binding energy (eV)	at.%	Binding energy (eV)	at.%	Binding energy (eV)	at. %
300	285.1	3.4	532.3	67.7	233.1	3.6	1221.1	25.2
310	284.7	4.0	532.7	69.2	232.7	4.6	1221.5	22.3
320	285.5	5.0	532.7	67.7	232.7	5.4	1221.5	22.0
330	284.9	7.2	532.9	67.7	232.9	6.8	1221.7	18.2
340	284.8	16.4	532.0	62.2	232.8	6.5	1221.6	14.9
350	285.2	9.5	532.4	65.4	232.4	8.6	1221.2	16.5
360	284.8	11.1	532.0	64.7	232.0	9.6	1221.6	14.6
370	285.2	13.4	532.4	61.0	231.6	10.9	1221.2	14.8
375	284.6	12.2	531.8	59.5	231.0	11.4	1220.6	16.9
380	285.3	22.4	531.7	47.5	229.3	14.8	1220.5	15.4

Analysis of the Mo 3d transitions (Fig. 9) shows quite different behavior compared to the Ge 3d transition. In contrast to the relative stability of the Ge^{4+} cation shown in Fig. 8, the Mo^{6+} cation ($BE_{3d5/2}$ = 233.0 eV) associated with octahedral MoO_3 observed for U_L = 300–320 V, partially reduced to Mo^{5+} ($BE_{3d5/2}$ = 231.3 eV) for a U_L of 340 V,

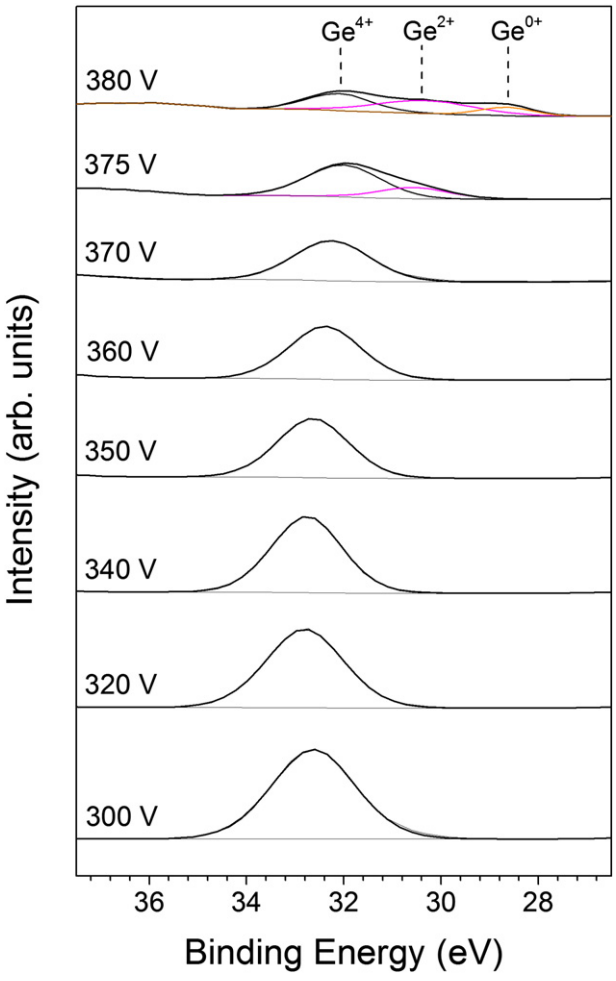

Fig. 8. High energy resolution XPS measurements of the Ge 3d transition for several values of U_L. Note that spectra for $U_L = 310$ and 330 were omitted due to similarity with $U_L = 300$ and 320. Gaussian–Lorentzian lineshapes, used for peak fitting, are overlaid (thin lines) upon the raw data (bold lines). Spectra are offset for clarity.

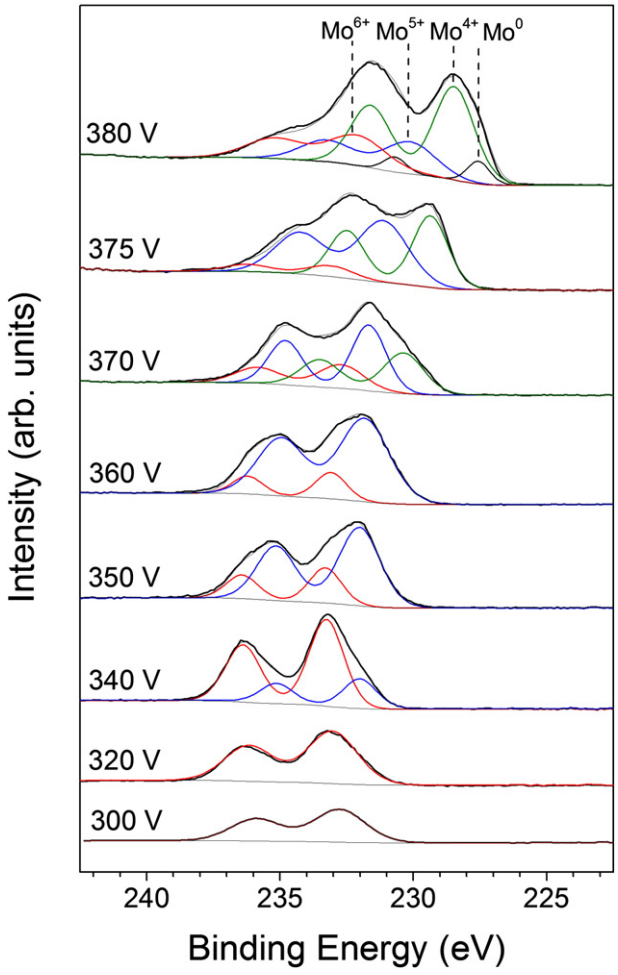

Fig. 9. High energy resolution XPS measurements of the Mo 3d transition for U_L values from 300–380 V. Spectra are offset for clarity. Note that spectra for $U_L = 310$ and 330 were omitted due to similarity with $U_L = 300$ and 320. Gaussian–Lorentzian lineshapes, used for peak fitting, are overlaid (thin lines) upon the raw data (bold lines). For simplicity, only the Mo $3d_{5/2}$ peaks are labeled.

indicating the presence of the intermediate surface compound Mo_2O_5 [38–40]. The concentration of Mo^{5+}, relative to Mo^{6+}, continues to increase from 15% to 85% as U_L is increased from 340 to 360 V. Formation of the Mo^{4+} cation ($BE_{3d5/2} = 229.2$ eV) occurs at $U_L > 360$ V, indicating the presence of tetrahedral MoO_2 in conjunction with MoO_3 and Mo_2O_5. Further increases in U_L lead to a larger fraction of Mo^{4+} at 375 V, with partial reduction to metallic Mo^0 occurring at 380 V, as evidenced by the presence of the Mo $3d_{5/2}$ component at 227.5 eV. Note that there is a variation in the binding energies of the Mo 3d doublets associated with Mo^{6+} and Mo^{5+}. An average binding energy associated with Mo^{6+} of 233.0 was measured for all values of U_L, with a maximum binding energy of 234.6 at $U_L = 370$ V and a minimum of 232.1 occurring at $U_L = 380$ V. Considering that these values have been calibrated to the adventitious C 1s transition at 284.6 (±0.1) eV, these deviations from published values for various Mo–O compounds are a possible indication of the presence of Mo–O–Ge compounds, or other complex chemistries. In addition, the augmented Mo^{6+} binding energies (233.0 to 234.5 eV) are similar to values (BE = 233.8) reported by Gil Rostra et al. attributed to a possible oxygen double bond within Mo^{6+} [15].

The effects of U_L on both the coordination chemistry, and the relative concentrations of the compounds present, are shown in Fig. 10. Fig. 10 illustrates the three main stages of reactive sputtering, namely, the (I) gettering, (II) transition, and (III) poisoned modes, indicating an excellent correlation between the onset of the transition sputtering mode and the formation of substoichiometric compounds.

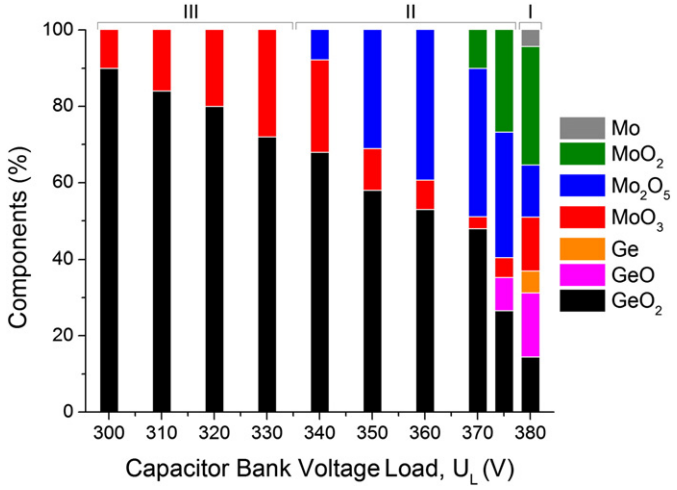

Fig. 10. Histogram depicting the relative amounts of germanium–oxygen and molybdenum–oxygen compounds as a function of capacitor bank voltage load (U_L).

The incremental changes in chemistry and composition brought on by systematic increases in U_L are shown to produce films with gradually increasing levels of optical absorption, as demonstrated in Fig. 11. As established through ligand field theory, and more recently, density functional theory, the coordination number and the arrangement of the metal–ligand bond have a significant effect on the electronic structure and subsequent optical behavior of the deposited films [23,24,36,39,75,77]. Qualitatively, films deposited from 300–320 V (Fig. 11a–c) are largely transparent with a subtle blue–gray coloration occurring at 310 V and 320 V, similar to coloration reported by Gil-Rostra et al. for mixed $Mo_xSi_yO_z$ thin films [15]. As U_L is increased further, the films take on a yellow hue (Fig. 11d–g), showing sensitivity to the increasing proportion of the surface phase Mo_2O_5. Subsequently, at U_L values from 370 V to 380 V (Fig. 11h–j), films demonstrate an evolution from dark yellow to a dark, highly absorbing appearance associated with the inclusion of MoO_2, Mo, and Ge in the films.

3.4. Optical characterization

The optical constants, *n* and *k*, and deposition rates of the $Mo_xGe_yO_z$ thin films were determined through measurement and simultaneous fitting of SE and T data. The model used within this work consists of a 1.65 mm quartz substrate, a general oscillator layer, and a Bruggeman effective medium layer, coupled to the general oscillator layer, consisting of 50% void fraction to account for the presence of surface roughness [59]. Raw data acquired through SE and T measurements were fit using a general oscillator model consisting of a Tauc–Lorentz oscillator (Eq. (1)) to account for the onset of the optical gap in the amorphous thin films and a Lorentz oscillator (Eq. (2)) to properly fit the observed absorption tail at energies beneath the optical gap [78,79]. For the film deposited at $U_L = 380$ V, one Tauc–Lorentz and two Lorentzo scillators were used in order to account for absorption features associated with the presence of elemental germanium and metallic molybdenum [78].

$$\epsilon_2(E) = 2nk = \frac{AE_oC(E-E_g)^2}{\left(E^2-E_o^2\right)^2 + C^2E^2}\cdot\frac{1}{E} \quad [79] \tag{1}$$

$$\tilde{n}(\lambda)^2 = 1 + \sum_j \frac{A\lambda^2}{\lambda^2-\lambda_o^2+iB\lambda} \quad [59] \tag{2}$$

In Eq. (1), A and C represent the amplitude and broadening terms of the Tauc–Lorentz oscillator, while E, E_o, and E_g are the photon energy,

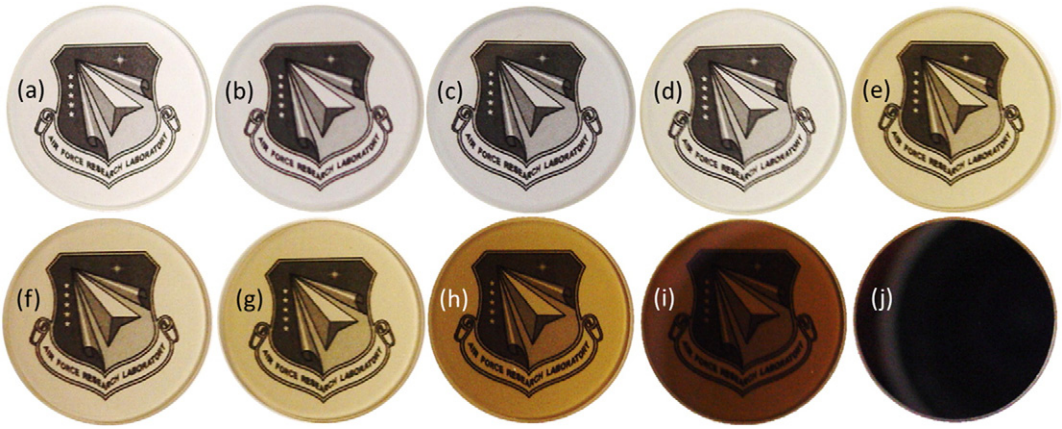

Fig. 11. Photograph of $Mo_xGe_yO_z$ films deposited on 25 mm diameter fused quartz substrates (a) 300 V, (b) 310 V, (c) 320 V, (d) 330 V, (e) 340 V, (f) 350 V, (g) 360 V, (h) 370 V, (i) 375 V, and (j) 380 V. Note the incremental changes in coloration associated with increases in U_L.

centroid, and optical gap, respectively [79]. The parameters A, B, and λ_o, represent the amplitude, broadening, and centroid of the Lorentz oscillator (Eq. (2)) [59]. Utilization of the Tauc–Lorentz oscillator is highly advantageous due to its ability to directly calculate E_g. Overlays of selected models and experimentally measured Ψ values at 50°, 55°, and 60° are shown in Fig. 12; associated transmission measurements are depicted in Fig. 13. A list of key fit parameters and model MSE values are shown in Table 4, note that the model MSE values are slightly elevated due to the simultaneous fitting of the SE and T data.

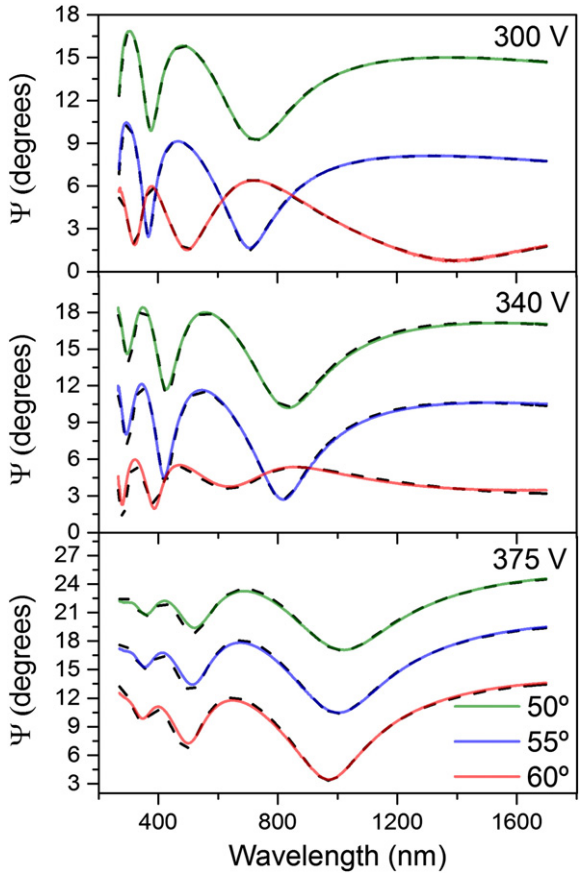

Fig. 12. Spectral response of the polarized light magnitude, Ψ, at 50°,55°, and 60°, for films deposited at U_L values of 300, 340, and 375. Associated model fits (dashed lines) are overlaid.

Film thicknesses and the corresponding deposition rates determined from XRR and SE measurements are shown in Fig. 14. Simultaneous modeling of SE and T data, and comparison with XRR thickness measurements, was performed in order to validate the fit quality, ensuring a unique solution for the thicknesses and optical constants. The thickness deposition rate shown in Fig. 14a indicates moderate change as a function of U_L, varying between 72 and 96 nm/min. The thickness deposition rates obtained via XRR and SE agree reasonably well. Film densities obtained from XRR were used to calculate the mass deposition rates and are shown in Fig. 14b. Note that densities were calculated assuming a uniform thickness over an area of 1 cm^2. The data in Fig. 14b illustrates a non-linear increase in the mass deposition rate as a function of U_L. The increased densification and associated mass deposition rates are the direct results of a higher molybdenum sputter yield brought on by the increases in the potential applied to the cathode [56,57,80]. Higher applied voltages produce increased kinetic energies of the incident Ar^+ ions, resulting in more sputtered atoms per ion collision [56,57,80]. Additionally, increases in the Mo sputter yields serve to decrease the oxygen partial pressure via chemisorption on the collecting surfaces of the chamber, leading to the deposition of substoichiometric compounds and elemental components.

The optical constants, *n* and *k*, for the $Mo_xGe_yO_z$ thin films are shown in Fig. 15a–b, respectively. The spectral behavior of both *n* and *k* indicates a dependence on the value of U_L used for deposition. For $U_L \leq 330$ V, *n* is relatively flat, ranging between 1.60 and 1.78 throughout the measured spectral region (380–1700 nm). A noticeable change in the dispersion, $n(\lambda)$, occurs at $U_L = 340$ V, wherein the value of *n* varies from 1.65 in the near IR to 1.85 at 255 nm. Sharp increases in both *n* and *k* at shorter wavelengths are characteristic of the onset of the absorption edge, correlating directly with the increased ratio of MoO_3 ($E_g = 2.8$–3.2 eV) [64,71,81] to GeO_2 ($E_g = 5.6$–5.9) [75,82,83] as determined by XPS. As evidenced by Fig. 15, increases in U_L, from 300 to 340 V, lead to higher *n* values, with *k* values gradually increasing towards the UV region. While the growth of *k* can be attributed to decreases in the optical gap energy, the spectral augmentation of *n* is likely the result of the deposition of higher density components, corresponding to increases in MoO_3 ($n_{589} = 2.2$) relative to GeO_2 ($n_{589} = 1.6$). The correlation between density (Fig. 6) and $n(\lambda)$ (Fig. 15a) is in line with the Lorentz–Lorenz relation [46,67]. U_L values from 340 to 375 V were associated with further increases in both *n* and *k*, indicating that the optical properties of the $Mo_xGe_yO_z$ films are significantly affected by small, incremental changes in U_L.

The calculation of the E_g values was performed by simultaneously modeling the SE and T data and extracting the E_g term from the Tauc–Lorentz component of the general oscillator layer (Eq. (1)). E_g

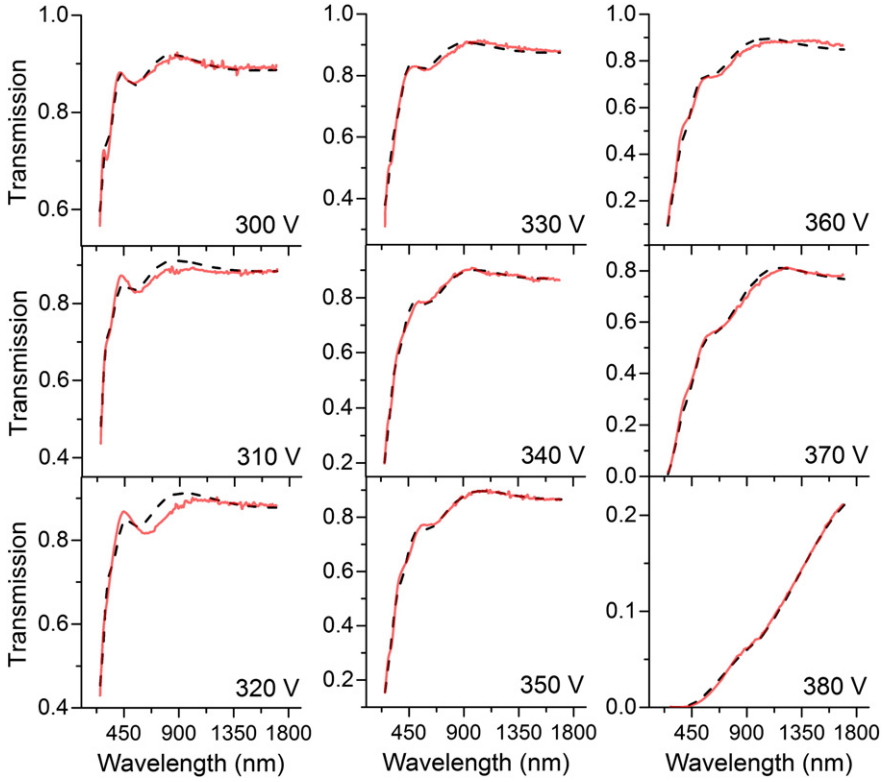

Fig. 13. VASE transmission plots for all deposited films and associated model fits (dashed lines). Note the excellent fit quality in the regions near the band edge λ < 400 nm. Scales are individually adjusted to allow for assessment of fit quality.

measurements were performed to determine the onset of inter-band absorption features correlated to the presence of different chemical species within the films. Due to the lack of long range crystalline order, as well as the large variety of valence states present within the $Mo_xGe_yO_z$ films, it would be difficult to fully parameterize the effect that each has upon the electronic structure of the films [84]. However, the combination of XRR, XPS, SE, and T measurements provides an adequate correlation between the optical and chemical properties of the films.

The chemical constituents, identified by XPS in Section 3.3, include GeO_2, GeO, Ge, MoO_3, Mo_2O_5, MoO_2, and Mo. These compounds and elements have different electronic structures, namely, wide E_g semiconductors in the case of GeO_2, GeO [72,73,75] and MoO_3 [29,64,85,86], semiconducting Ge [87], and electrically conductive materials such as Mo and MoO_2 [39,77,88–91]. Published values for the band energies of each of the chemical constituents present are listed in Table 5. The VASE transmission plots, and overlaid model calculations, shown in Fig. 13 indicate large changes in the optical properties of the $Mo_xGe_yO_z$ films of as a function of U_L.

Table 4
Mean squared error (MSE), thickness, roughness, and E_g values measured using variable angle spectroscopic ellipsometry.

U_L (V)	Error (MSE)	Thickness (nm)	Roughness (nm)	E (eV)
300	9.76	251	3.3	3.57 ± 0.04
310	12.88	251	0.6	3.36 ± 0.05
320	22.58	267	3.5	3.35 ± 0.08
330	13.13	264	3.0	2.97 ± 0.04
340	19.54	271	2.9	1.61 ± 0.03
350	15.85	276	3.4	1.27 ± 0.05
360	17.98	277	3.8	0.84 ± 0.07
370	18.53	265	4.6	0.18 ± 0.02
375	20.84	260	6.9	0.00 ± 0.01
380	8.34	214	6.8	0.00 ± 0.45

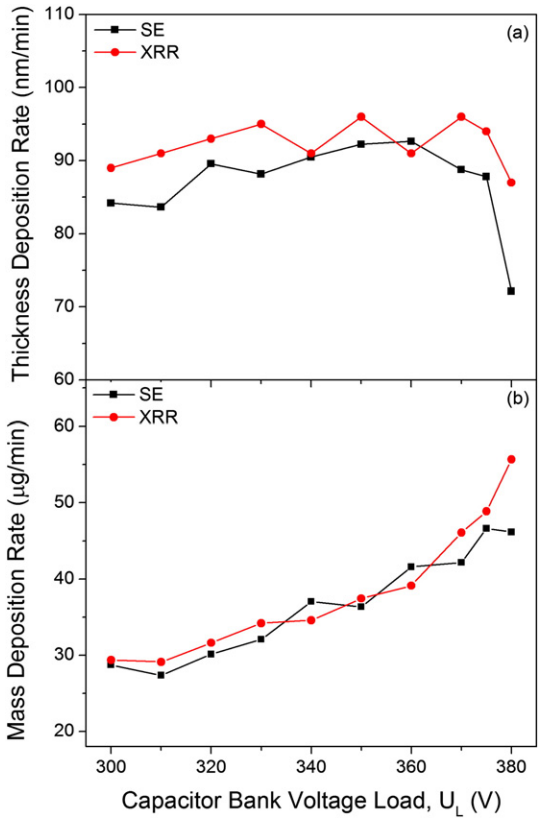

Fig. 14. Deposition rates as calculated from XRR and SE analysis. a) Thickness deposition rates as a function of U_L. b) Mass deposition rates as a function of U_L. Deposition time for these samples was 1 min.

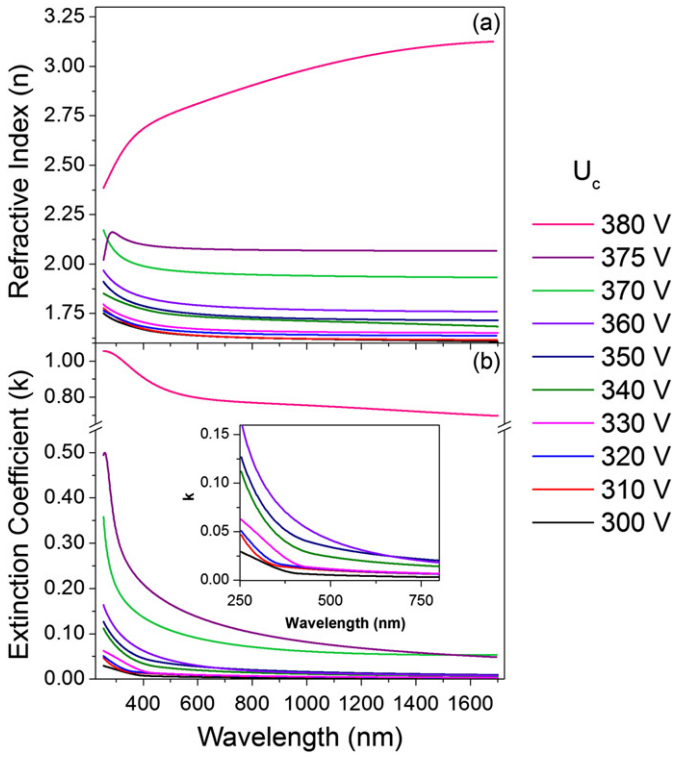

Fig. 15. Plot of the refractive index (a) and extinction coefficient (b) as a function of wavelength for the different capacitor bank voltage load values (U_L).

The onset of band-to-band absorption is easily identifiable by the precipitous drops in transmission shown in Fig. 13, and by the systematic increases in *k* towards the UV region depicted by Fig. 15b. Given the high quality of the fitting within both Figs. 12 and 13, especially in the wavelength region encompassing the band edge, it is evident that the Tauc–Lorentz oscillator calculation provides an accurate estimation of E_g. Interestingly, the E_g values for films deposited within the poisoned regime ($U_L \leq 330$ V) (Table 4) are significantly lower than values for bulk germanium oxide (Table 5) ($5.9 \leq E_g \leq 6$) [72,73,75,83]; this is likely due to the presence of MoO_3 and is potential result of the formation of Mo–O–Ge bonds. Similar complex bonding structures, involving oxygen sharing between octahedral metal oxides and tetrahedral oxides of both SiO_2 [15] and GeO_2 [92] have been reported for reactively sputtered mixed oxide compounds. When compared with XPS data, the gradual decrease in E_g from 3.57 (±0.04) at $U_L = 300$ V to 2.97 eV (±0.04) at $U_L = 330$ eV is associated with an 18% increase in MoO_3 (Mo^{6+}) content. Upon entering the transition regime (II), E_g changes rapidly for U_L values of 340, 350 and 360 V, corresponding to values of 1.61 (±0.03), 1.27 (±0.05), and 0.84 eV (±0.07), respectively. The large change observed in E_g from 340–360 V indicates that E_g is significantly affected by the 32% increase of the surface phase Mo_2O_5 (Mo^{5+}) and associated oxygen vacancies. Further increases in U_L, from 370 to 375 V are characterized by a decrease in E_g, from 0.18 (±0.02) to 0.00 eV (±0.01), respectively. This marked decrease in E_g at 370 and 375 V is directly related to the presence of MoO_2 (Mo^{4+}) and, concurrently, GeO (Ge^{2+}). An E_g of 0.00 (±0.45) eV, was also found to occur at $U_L = 380$ V, a result that is in line with the presence of 4% Mo and 30% MoO_2. Note that XPS also detected the presence of nearly 6% Ge, as shown in Fig. 10. Investigation of the relationship between E_g and U_L has indicated that increases in U_L can be correlated to decreases in the magnitude of E_g, the behavior of which is intimately coupled with P_{O2}, as illustrated in Fig. 16. A detailed physical explanation of the changes in E_g, as a function of the processing parameter U_L, is presented and discussed in the next section.

Table 5
List of published band gaps for selected oxides of germanium and molybdenum.

	Oxidation state	Compound	Band gap, E_g (eV)	Reference no.
Ge	0	Ge	0.67–0.88	[72,73,75]
	2+	GeO[a]	2.8–4.0	[75,95]
	4+	GeO_2	5.9–6.1	[72,73,75,86]
Mo	0	Mo	0	
	4+	MoO_2	0	[39,92–94]
	5+	Mo_2O_5[b]	N/A	
	6+	MoO_3	2.7–3.2	[64,84,96,97]

[a] Band gaps are from numerical simulations.
[b] Note that Mo_2O_5 is classified as a "surface phase" with no known bulk structure [38–40].

3.5. Process-optical property correlation

Studies of the optical behavior, focusing on *n*, *k*, and E_g, have indicated incremental changes associated with decreases in P_{O2} as a result of increasing U_L. The films' coloration can be directly attributed to the magnitude of E_g, as no other dominant absorption features are shown within visible wavelengths, as was shown in Fig. 15b. One trend that is particularly noteworthy is the correlation between film chemistry and E_g. Based on the complex chemistry and the amorphous structure of the films, it is difficult to quantitatively parameterize the effect of each coordination compound on the resulting band structure. However, through the use of principles set forth by ligand field theory, a comprehensive, albeit qualitative, explanation of the decrease in E_g with increasing U_L can be reached. As depicted in Figs. 10 and 16, it is evident that each large change in E_g can be associated with a change in coordination chemistry, with the exception of films deposited within the poisoned regime (III) where the properties can be correlated to the existence of fully stoichiometric MoO_3 and GeO_2. The transparent films, $E_g = 3.57$ eV (±0.04), deposited at a U_L of 300 V are a direct result of the large E_g values associated with Mo^{6+} and Ge^{4+} coordination compounds. The large E_g of MoO_3 is the result of the splitting of 4d orbitals attributed to the static electric field between the 6 O^{2-} anions surrounding the central Mo^{6+} cation, leading to a MoO_6 octahedral base unit [7]. The resulting metal–ligand bonding between Mo and O leads to the splitting of the Mo 4d levels into anti-bonding t_{2g} and bonding e_g sets. These anti-bonding t_{2g} sets are unfilled in MoO_3, resulting in an energy gap of 2.7–3.2 eV between the Mo 4d (t_{2g}) and O 2p ($p\pi$) levels [7,38,93,94]. Note that GeO_2, based on the tetrahedral GeO_4 structural unit, has an E_g of 5.9–6.1 eV, thus rendering it incapable of absorbing visible wavelengths. As U_L is increased further, to 310 and 320 V, a slight blue–gray tint is

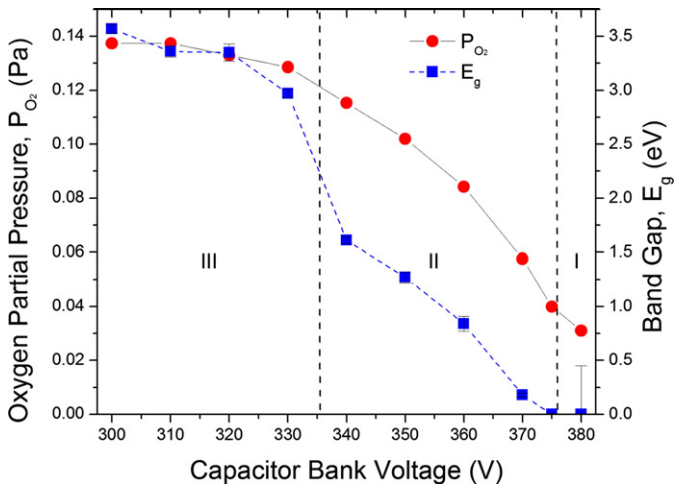

Fig. 16. Calculated values of E_g for U_L from 300 to 380 V. The vertical dotted lines are included to signify the onset of the (III) poisoned, (II) transition, and (I) gettering modes associated with reactive sputtering.

observed, corresponding to E_g values of 3.36 (±0.05) and 3.35 (±0.08) eV. Previous studies have observed blue coloration in slightly reduced MoO_3 films with oxygen vacancies, denoted as MoO_{3-x} [15,38,94]. The mechanism attributed to the blue coloration of MoO_{3-x} has been related to the onset of free carrier absorption as a result of electrons being excited to the previously unfilled t_{2g} band [7,38,94]. Increasing U_L to 330 V corresponds to films with an E_g of 2.97 (±0.04) eV, leading to a yellow tint associated with the increased Mo:Ge ratio. An E_g near 2.8 eV is near the lower bound of those reported for MoO_3 [29,64], and is related to absorption of blue light ($\lambda < 440$ eV), leading to a yellow coloration [36,95]. The yellow hue of the films persists, becoming more intense within the transition regime (II) for U_L values of 340 to 360, and is correlated to an increase in the amount of Mo_2O_5 (Fig. 10). As the amount of Mo_2O_5 increases from 340 to 360 V, the slope of associated transmission curves also becomes more gradual. Decreases in the slope of transmission curves (Fig. 13) can be attributed to the augmentation of electron–electron and impurity scattering events related to increased doping levels in indirect semiconductors [84]. The slope, and magnitude of the transmission curves continue to decrease alongside U_L related to increases in $Mo^{x<6+}$ and $Ge^{x<4+}$ cation concentration. Further decreases in E_g occur for U_L settings of 370 to 375 V, as a result of reaching P_{O2} values conducive to the formation of MoO_2. MoO_2 is reported to have metal-like conductivity as a result of Mo–Mo bond formation [39]. GeO is also present within films deposited where $U_L \geq 370$ V, and GeO has been reported to have calculated E_g values ranging from 2.8–4.0 eV [75,96], potentially bolstering the yellow appearance associated with E_g values near 2.8 eV. Finally, the film deposited at $U_L = 380$ V has minimal optical transparency as a result of the presence of elemental Mo and Ge.

4. Summary and conclusions

Based upon the results presented within this study, it is evident that the optical absorption, and correspondingly, the coloration of amorphous $Mo_xGe_yO_z$ thin films can be systematically varied by modifying the MPPMS capacitor bank voltage, U_L. Increases in U_L have been shown to decrease P_{O2} due to the oxygen chemisorption from the high fraction of Mo within the MPPMS deposition flux. As shown from the XPS measurements and peak fitting, decreases in P_{O2} are directly related to increases in the ratio of Mo to Ge within the deposition flux and film densification associated with the presence of substoichiometric compounds including GeO (Ge^{2+}), Mo_2O_5 (Mo^{5+}), and MoO_2 (Mo^{4+}). Furthermore, the presence, and relative amounts, of the different coordination complexes can be directly correlated to decreases in both P_{O2} and E_g. The process–property relationship between U_L and E_g, established within this work, allows for the deposition of $Mo_xGe_yO_z$ films with E_g values that are able to be tailored between 3.4 and 0.4 eV. In addition, analysis of the optical constants obtained from spectroscopic ellipsometry also indicated incremental increases in both n and k, as a function of increasing U_L. The high degree of control available for both n and k shows promise in the design and fabrication of multilayer interference coatings that require precise control over the optical constants. The hybrid DC-MPPMS co-deposition method used in this work has been shown to be a highly controllable, scalable method for depositing mixed-valent ionic glass coatings with absorption features spanning the breadth of the visible spectrum.

References

[1] Y. Okuhara, T. Kato, H. Matsubara, N. Isu, M. Takata, Near-infrared reflection from periodically aluminium-doped zinc oxide thin films, Thin Solid Films 519 (2011) 2280–2286.
[2] T. Minami, H. Nanto, S. Takata, Highly conductive and transparent aluminum doped zinc oxide thin films prepared by RF magnetron sputtering, Jpn. J. Appl. Phys. 23 (1984) L280.
[3] T. Minami, Present status of transparent conducting oxide thin-film development for indium–tin-oxide (ITO) substitutes, Thin Solid Films 516 (2008) 5822–5828.
[4] I. Hamberg, C.G. Granqvist, Evaporated Sn doped In_2O_3 films: basic optical properties and applications to energy efficient windows, J. Appl. Phys. 60 (1986) R123–R160.
[5] W.G. Haines, R.H. Bube, Effects of heat treatment on the optical and electrical properties of indium–tin oxide films, J. Appl. Phys. 49 (1978) 304–307.
[6] Y. Ji, S. Li, G.A. Niklasson, C.G. Granqvist, Durability of thermochromic VO_2 thin films under heating and humidity: effect of Al oxide top coatings, Thin Solid Films 562 (2014) 568–573.
[7] C. Granqvist, Electrochromic oxides: a bandstructure approach, Sol. Energy Mater. Sol. Cells 32 (1994) 369–382.
[8] C.G. Granqvist, Handbook of Inorganic Electrochromic Materials, Elsevier Science, 1995.
[9] J. Coleman, J. Freeman, P. Madhukar, J. Wagenknecht, Electrochromism of nanoparticulate-doped metal oxides: optical and material properties, Displays 20 (1999) 145–154.
[10] B.H. Lee, I.G. Kim, S.W. Cho, S. Lee, Effect of process parameters on the characteristics of indium tin oxide thin film for flat panel display application, Thin Solid Films 302 (1997) 25–30.
[11] D. Corr, U. Bach, D. Fay, M. Kinsella, C. McAtamney, F. O'Reilly, S. Rao, N. Stobie, Coloured electrochromic "paper-quality" displays based on modified mesoporous electrodes, Solid State Ionics 165 (2003) 315–321.
[12] J. Liu, J.P. Coleman, Nanostructured metal oxides for printed electrochromic displays, Mater. Sci. Eng. A 286 (2000) 144–148.
[13] W.H. Southwell, R.L. Hall, Rugate filter sidelobe suppression using quintic and rugated quintic matching layers, Appl. Opt. 28 (1989) 2949–2951.
[14] W.E. Johnson, R.L. Crane, Introduction to rugate filter technology, Proc. SPIE 2046 (1993) 88–108.
[15] J. Gil-Rostra, J. Chaboy, F. Yubero, A. Vilajoana, A.R. Gonzalez-Elipe, Colored and transparent oxide thin films prepared by magnetron sputtering: the glass blower approach, ACS Appl. Mater. Interfaces 5 (2013) 1967–1976.
[16] F. Gracia, F. Yubero, J. Holgado, J. Espinos, A. Gonzalez-Elipe, T. Girardeau, SiO_2TiO_2 thin films with variable refractive index prepared by ion beam induced and plasma enhanced chemical vapor deposition, Thin Solid Films 500 (2006) 19–26.
[17] J. Gil-Rostra, M. Cano, J.M. Pedrosa, F.J. Ferrer, F. García-García, F. Yubero, A.R. González-Elipe, Electrochromic behavior of $W_xSi_yO_z$ thin films prepared by reactive magnetron sputtering at normal and glancing angles, ACS Appl. Mater. Interfaces 4 (2012) 628–638.
[18] J. Gil-Rostra, F. Yubero, R. Fernández, T. Vilajoana, P. Artús, J. Dürsteler, J. Cotrino, I. Ortega, A. González-Elipe, Colored semi-transparent Cu–Si oxide thin films prepared by magnetron sputtering, Opt. Mater. Express 1 (2011) 1100–1112.
[19] J. Gil-Rostra, F. García-García, F. Yubero, A.R. González-Elipe, Tuning the transmittance and the electrochromic behavior of $Co_xSi_yO_z$ thin films prepared by magnetron sputtering at glancing angle, Sol. Energy Mater. Sol. Cells 123 (2014) 130–138.
[20] A. Terczynska-Madej, K. Cholewa-Kowalska, M. Laczka, The effect of silicate network modifiers on colour and electron spectra of transition metal ions, Opt. Mater. 32 (2010) 1456–1462.
[21] M. Łączka, K. Cholewa, Chromium, cobalt, nickel and copper as pigments of sol–gel glasses, J. Alloys Compd. 218 (1995) 77–85.
[22] M. Łączka, K. Cholewa, W. Mozgawa, Glass-crystalline materials of the $CaO–P_2O_5–SiO_2$ system obtained by the sol–gel method, J. Mater. Sci. Lett. 14 (1995) 1417–1420.
[23] J.E. Shelby, Introduction to Glass Science and Technology, Royal Society of Chemistry, 2005.
[24] K. Nassau, The Physics and Chemistry of Color: The Fifteen Causes of Color, 2nd ed. Wiley VCH, 2001 496.
[25] J.G. Rostra, J.C.D. López, A.V. Mas, A. Rodriguez-González-Elipe, R.F. Serrano, F.Y. Valencia, Polymeric based lens comprising a hardening layer, an absorbent layer and interferential multi-layer and corresponding manufacturing method. US Patent (2010).
[26] M. Arvizu, C. Triana, B. Stefanov, C. Granqvist, G. Niklasson, Electrochromism in sputter-deposited W–Ti oxide films: durability enhancement due to Ti, Sol. Energy Mater. Sol. Cells 125 (2014) 184–189.
[27] M. Arvizu, M. Morales-Luna, S. Tomás, P. Rodríguez, O. Zelaya-Angel, Photochromism and thermochromism of MoO thin films doped with ZnSe, AIP Conf. Proc. 1420 (2012) 151.
[28] C. Battaglia, X. Yin, M. Zheng, I.D. Sharp, T.L. Chen, A. Azcatl, S. McDonell, C. Carraro, R. Maboudian, R.M. Wallace, Hole selective MoO_x contact for silicon solar cells, Nano Lett. 14 (2014) 967–971.
[29] T.S. Sian, G. Reddy, Optical, structural and photoelectron spectroscopic studies on amorphous and crystalline molybdenum oxide thin films, Sol. Energy Mater. Sol. Cells 82 (2004) 375–386.
[30] X. Jiang, F. Wong, M. Fung, S. Lee, Aluminum-doped zinc oxide films as transparent conductive electrode for organic light-emitting devices, Appl. Phys. Lett. 83 (2003) 1875–1877.
[31] H. Kim, A. Pique, J. Horwitz, H. Murata, Z. Kafafi, C. Gilmore, D. Chrisey, Effect of aluminum doping on zinc oxide thin films grown by pulsed laser deposition for organic light-emitting devices, Thin Solid Films 377 (2000) 798–802.
[32] H. Kim, C. Gilmore, A. Pique, J. Horwitz, H. Mattoussi, H. Murata, Z. Kafafi, D. Chrisey, Electrical, optical, and structural properties of indium–tin-oxide thin films for organic light-emitting devices, J. Appl. Phys. 86 (1999) 6451–6461.
[33] A. Tsiatmas, A. Buckingham, V. Fedotov, S. Wang, Y. Chen, P. De Groot, N. Zheludev, Superconducting plasmonics and extraordinary transmission, Appl. Phys. Lett. 97 (2010) 111106.
[34] G.V. Naik, V.M. Shalaev, A. Boltasseva, Alternative plasmonic materials: beyond gold and silver, Adv. Mater. 25 (2013) 3264–3294.
[35] U. Guler, G. Naik, A. Boltasseva, V. Shalaev, A. Kildishev, Nitrides as alternative materials for localized surface plasmon applications, FiO/LS Technical Digest2012 FTh4A2.

[36] S.K. Shevell, The Science of Color, Elsevier, 2003.
[37] D.R. Lide, CRC Handbook of Chemistry and Physics 2004–2005: A Ready-reference Book of Chemical and Physical Data, CRC press, 2004.
[38] F. Werfel, E. Minni, Photoemission study of the electronic structure of Mo and Mo oxides, J. Phys. C 16 (2000) 6091.
[39] D.O. Scanlon, G.W. Watson, D. Payne, G. Atkinson, R. Egdell, D. Law, Theoretical and experimental study of the electronic structures of MoO_3 and MoO_2, J. Phys. Chem. C 114 (2010) 4636–4645.
[40] O. Marin-Flores, L. Scudiero, S. Ha, X-ray diffraction and photoelectron spectroscopy studies of MoO_2 as catalyst for the partial oxidation of isooctane, Surf. Sci. 603 (2009) 2327–2332.
[41] C. Ramana, G. Baghmar, E.J. Rubio, M.J. Hernandez, Optical constants of amorphous, transparent titanium-doped tungsten oxide thin films, ACS Appl. Mater. Interfaces 5 (2013) 4659–4666.
[42] Y. Chen, T. Lin, T. Chen, Y. Li, K. Weng, Electrochromic properties of tungsten–titanium oxide films, J. Nanosci. Nanotechnol. 12 (2012) 1296–1300.
[43] T. Karasawa, Y. Miyata, Electrical and optical properties of indium tin oxide thin films deposited on unheated substrates by DC reactive sputtering, Thin Solid Films 223 (1993) 135–139.
[44] N. Miyata, K. Miyake, Y. Yamaguchi, Cadmium–tin-oxide films deposited by dc reactive sputtering from a Cd–Sn alloy target, Appl. Phys. Lett. 37 (1980) 180–182.
[45] N. Tsukamoto, S. Sensui, J. Jia, N. Oka, Y. Shigesato, Study on reactive sputtering to deposit transparent conductive amorphous In_2O_3–ZnO films using an In–Zn alloy target, Thin Solid Films 559 (2014) 49–52.
[46] M. Vargas, E. Rubio, A. Gutierrez, C. Ramana, Spectroscopic ellipsometry determination of the optical constants of titanium-doped WO_3 films made by co-sputter deposition, J. Appl. Phys. 115 (2014) 133511.
[47] H. Yuanrong, W. Lige, L. Guoqing, Electrochromic properties of sputtered Ti-doped WO_3 films, Plasma Sci. Technol. 9 (2007) 452.
[48] D. Singh, S. Singh, U. Kumar, R. Srinivasa, S. Major, Transparent conducting Ga-doped ZnO thin films grown by reactive co-sputtering of Zn and GaAs, Thin Solid Films 555 (2014) 126–130.
[49] C.H. Ong, H. Gong, Effects of aluminum on the properties of p-type Cu–Al–O transparent oxide semiconductor prepared by reactive co-sputtering, Thin Solid Films 445 (2003) 299–303.
[50] M. Hála, J. Čapek, O. Zabeida, J. Klemberg-Sapieha, L. Martinu, Hysteresis-free deposition of niobium oxide films by HiPIMS using different pulse management strategies, J. Phys. D 45 (2012) 055204.
[51] W.D. Sproul, D.J. Christie, D.C. Carter, Control of reactive sputtering processes, Thin Solid Films 491 (2005) 1–17.
[52] W.D. Sproul, J. Lin, J.J. Moore, Mass/Energy Analysis of a Modulated Pulse Power Plasma Compared to a DC Plasma, SVC Spring Bulletin, 2009 28.
[53] J. Lin, W.D. Sproul, J.J. Moore, Z. Wu, S. Lee, R. Chistyakov, B. Abraham, Recent advances in modulated pulsed power magnetron sputtering for surface engineering, JOM 63 (2011) 48–58.
[54] J. Lin, W.D. Sproul, J.J. Moore, S. Lee, S. Myers, High rate deposition of thick CrN and Cr_2N coatings using modulated pulse power (MPP) magnetron sputtering, Surf. Coat. Technol. 205 (2011) 3226–3234.
[55] D. Depla, R. De Gryse, Target poisoning during reactive magnetron sputtering: Part I: the influence of ion implantation, Surf. Coat. Technol. 183 (2004) 184–189.
[56] S. Berg, T. Nyberg, Fundamental understanding and modeling of reactive sputtering processes, Thin Solid Films 476 (2005) 215–230.
[57] S. Berg, E. Särhammar, T. Nyberg, Upgrading the "Berg-model" for reactive sputtering processes, Thin Solid Films 476 (2014) 215–230.
[58] Neal Fairley, Casa Software Ltd. CasaXPS 2.3.16, 1999–2011.
[59] CompleteEASE™ Data Analysis Manual Version 4.05, J.A. Woollam Co., Inc., 2009
[60] D. Guttler, B. Abendroth, R. Grotzschel, W. Moller, D. Depla, Mechanisms of target poisoning during magnetron sputtering as investigated by real-time in situ analysis and collisional computer simulation, Appl. Phys. Lett. 85 (2004) 6134–6136.
[61] D. Depla, R. De Gryse, Target poisoning during reactive magnetron sputtering: part II: the influence of chemisorption and gettering, Surf. Coat. Technol. 183 (2004) 190–195.
[62] D. Depla, S. Heirwegh, S. Mahieu, J. Haemers, R. De Gryse, Understanding the discharge voltage behavior during reactive sputtering of oxides, J. Appl. Phys. 101 (2007) 013301.
[63] J. Lin, J.J. Moore, W.D. Sproul, S.L. Lee, J. Wang, Effect of negative substrate bias on the structure and properties of Ta coatings deposited using modulated pulse power magnetron sputtering, IEEE Trans. Plasma Sci. 38 (2010) 3071–3078.
[64] S. Mohamed, O. Kappertz, J. Ngaruiya, T. Leervad Pedersen, R. Drese, M. Wuttig, Correlation between structure, stress and optical properties in direct current sputtered molybdenum oxide films, Thin Solid Films 429 (2003) 135–143.
[65] I. Petrov, P. Barna, L. Hultman, J. Greene, Microstructural evolution during film growth, J. Vac. Sci. Technol. A 21 (2003) S117–S128.
[66] P. Barna, M. Adamik, Fundamental structure forming phenomena of polycrystalline films and the structure zone models, Thin Solid Films 317 (1998) 27–33.
[67] N. Kaiser, Review of the fundamentals of thin-film growth, Appl. Opt. 41 (2002) 3053–3060.
[68] W. Hume-Rothery, H.M. Powell, On the theory of super-lattice structures in alloys, Z. Kristallogr. 91 (1935) 23–47.
[69] U. Mizutani, Hume-Rothery Rules for Structurally Complex Alloy Phases, CRC Press, 2010.
[70] M. Yasaka, X-ray thin-film measurement techniques, V. X-ray reflectivity measurement, Rigaku J. 26 (2010) 1–9.
[71] V. Nirupama, K. Gunasekhar, B. Sreedhar, S. Uthanna, Effect of oxygen partial pressure on the structural and optical properties of dc reactive magnetron sputtered molybdenum oxide films, Curr. Appl. Phys. 10 (2010) 272–278.
[72] T. Lange, W. Njoroge, H. Weis, M. Beckers, M. Wuttig, Physical properties of thin GeO_2 films produced by reactive DC magnetron sputtering, Thin Solid Films 365 (2000) 82–89.
[73] F. Vega, J. De Sande, C. Afonso, C. Ortega, J. Siejka, Optical properties of GeO_x films obtained by laser deposition and dc sputtering in a reactive atmosphere, Appl. Opt. 33 (1994) 1203–1208.
[74] N. Murphy, J. Grant, L. Sun, J. Jones, R. Jakubiak, V. Shutthanandan, C. Ramana, Correlation between optical properties and chemical composition of sputter-deposited germanium oxide (GeO_x) films, Opt. Mater. 36 (2014) 1177–1182.
[75] L. Lin, K. Xiong, J. Robertson, Atomic structure, electronic structure, and band offsets at Ge:GeO:GeO_2 interfaces, Appl. Phys. Lett. 97 (2010) 242902.
[76] J.F. Binder, P. Broqvist, A. Pasquarello, Electron trapping in substoichiometric germanium oxide, Appl. Phys. Lett. 97 (2010) 092903.
[77] V. Eyert, R. Horny, K. Höck, S. Horn, Embedded Peierls instability and the electronic structure of MoO_2, J. Phys. D 12 (2000) 4923.
[78] E.D. Palik, Handbook of Optical Constants of Solids, Academic press, 1998.
[79] G. Jellison, F. Modine, Parameterization of the optical functions of amorphous materials in the interband region, Appl. Phys. Lett. 69 (1996) 371–373.
[80] J. Ziegler, SRIM & TRIM user's manual, www.srim.org2008.
[81] T. He, J. Yao, Photochromism of molybdenum oxide, J. Photochem. Photobiol. C 4 (2003) 125–143.
[82] A. Ohta, H. Nakagawa, H. Murakami, S. Higashi, S. Miyazaki, Photoemission study of ultrathin GeO_2/Ge heterostructures formed by UV-O_3 oxidation, e-J. Surf. Sci. Nanotechnol. 4 (2006) 174–179.
[83] M. Perego, G. Scarel, M. Fanciulli, I. Fedushkin, A. Skatova, Fabrication of GeO_2 layers using a divalent Ge precursor, Appl. Phys. Lett. 90 (2007) 162115.
[84] J.I. Pankove, Optical Processes in Semiconductors, Dover Publications, New York, 1971 34.
[85] T. He, H. Yao, Photochromism in transition-metal oxides, Res. Chem. Intemediat. 40 (2004) 459–488.
[86] C.G. Granqvist, Handbook of Inorganic Electrochromic Materials, Elsevier, 1995.
[87] J. Tauc, R. Grigorovici, A. Vancu, Optical properties and electronic structure of amorphous germanium, Physica Status Solidi B 15 (1966) 627–637.
[88] A. Katrib, J. Sobczak, M. Krawczyk, L. Zommer, A. Benadda, A. Jablonski, G. Maire, Surface studies and catalytic properties of the bifunctional bulk MoO_2 system, Surf. Interface Anal. 34 (2002) 225–229.
[89] L. Yang, Q. Gao, Y. Tang, Y. Wu, R. Holze, MoO_2 synthesized by reduction of MoO_3 with ethanol vapor as an anode material with good rate capability for the lithium ion battery, J. Power Sources 179 (2008) 357–360.
[90] Y. Shi, B. Guo, S.A. Corr, Q. Shi, Y. Hu, K.R. Heier, L. Chen, R. Seshadri, G.D. Stucky, Ordered mesoporous metallic MoO_2 materials with highly reversible lithium storage capacity, Nano Lett. 9 (2009) 4215–4220.
[91] A. Bandi, Electrochemical reduction of carbon dioxide on conductive metallic oxides, J. Electrochem. Soc. 137 (1990) 2157–2160.
[92] C. Lu, C.H. Lee, W. Zhang, T. Nishimura, K. Nagashio, A. Toriumi, Structural and thermodynamic consideration of metal oxide doped GeO_2 for gate stack formation on germanium, J. Appl. Phys. 116 (2014) 174103.
[93] N. Miyata, S. Akiyoshi, Preparation and electrochromic properties of rf-sputtered molybdenum oxide films, J. Appl. Phys. 58 (1985) 1651–1655.
[94] G. Mountjoy, J. Yuan, P. Gaskell, Electron energy loss near edge spectroscopy of oxygen in amorphous and crystalline WO_3 and MoO_3, Inst. Phys. Conf. Ser. 138 (1993) 35–38.
[95] R. Juryska, Optical absorption and electronic transitions in MoO_3 single crystals, Phys. Status Solidi B 72 (1975) 161–164.
[96] S. Kar, S. Van Elshocht, K. Kita, M. Houssa, D. Misra, Physics and technology of high-k materials, ECS Trans. 40 (2011) 283–292.
[97] N.R. Murphy, L. Sun, J.T. Grant, J.G. Jones, R. Jakubiak, Molybdenum Oxides Deposited by Modulated Pulse Power Magnetron Sputtering: Stoichiometry as a Function of Process Parameters, J. Electron. Mater. (2015) http://dx.doi.org/10.1007/s11664-015-3790-9.